

Learning Ecological and Epidemic Processes using Neural ODEs, Kolmogorov–Arnold Network ODEs and SINDy

Maria Vasilyeva * Zheng Wei* Kelum Gajamannage[†] Hyangim Ji*
Aleksei Krasnikov* Alexey Sadovski*

January 16, 2026

Abstract

We consider epidemic and ecological models to investigate their coupled dynamics. Starting with the classical Susceptible–Infected–Recovered (SIR) model for basic epidemic behavior and the predator–prey (Lotka–Volterra, LV) system for ecological interactions, we then combine these frameworks into a coupled Lotka–Volterra–Susceptible–Infected–Susceptible (LVSIS) model. The resulting system consists of four differential equations describing the evolution of susceptible and infected prey and predator populations, incorporating ecological interactions, disease transmission, and spatial dispersal. To learn the underlying dynamics directly from data, we employ several data-driven modeling frameworks: Neural Ordinary Differential Equations (Neural ODEs), Kolmogorov–Arnold Network Ordinary Differential Equations (KANODEs), and Sparse Identification of Nonlinear Dynamics (SINDy). Numerical experiments based on synthetic data are conducted to investigate the learning ability of these models in capturing the epidemic and ecological behavior. We further extend our approach to spatio-temporal models, aiming to uncover hidden local couplings.

1 Introduction

Ecological and epidemic systems play a crucial role in shaping population survival, maintaining biodiversity, and ensuring ecosystem stability [1, 2, 3, 4]. Classical predator–prey models, such as the Lotka–Volterra system, describe fundamental ecological interactions of growth, mortality, and predation, while epidemic models like the Susceptible – Infected – Recovered frameworks capture disease transmission within populations. When these frameworks are coupled, they form eco-epidemic models that simultaneously account for trophic interactions and infection dynamics [5]. The resulting dynamics are nonlinear and exhibit complex behaviors, depending on ecological parameters and infection rates. In many real-world applications, uncovering the exact parameters of ecological and epidemiological models is often extremely challenging. Growth rates, predation intensities, transmission coefficients, and diffusion coefficients can vary across environments and are rarely measurable with precision. Moreover, the true mechanisms governing population and disease interactions are frequently more complicated than those described by classical differential equation models. As a result, model misspecification and parameter uncertainty limit the predictive power of traditional approaches. To address these difficulties, we employ a data-driven framework to learn system dynamics directly from observations. Recent advances in data-driven modeling have enabled the discovery of governing equations directly from time-series data [6, 7].

Several neural network architectures have been developed to complement or replace classical equation-based approaches, particularly in the context of epidemic modeling. Neural networks (NNs) provide

*Department of Mathematics and Statistics, Texas A&M University–Corpus Christi, Corpus Christi, TX, USA
Email: maria.vasilyeva@tamucc.edu.

[†]Department of Mathematics and Applied Mathematical Sciences, University of Rhode Island, Kingston, RI, USA
Email: kelum.gajamannage@uri.edu.

flexible frameworks capable of capturing the complex nonlinear dynamics commonly observed in epidemics [8]. Neural ODEs have been introduced for modeling epidemic dynamics, providing a continuous-time framework that naturally aligns with the underlying differential equation structure of epidemic processes [9, 10]. Epi-DNN employs deep neural networks to estimate time-varying or unknown parameters of traditional epidemic models, such as transmission and recovery rates [11]. The Long Short-Term Memory (LSTM) algorithm, which uses a type of recurrent neural network (RNN), was previously used in other studies to predict infections over time [12, 13]. Neural networks have been successfully applied in ecology to model species distributions and predict ecological outcomes. Convolutional Neural Networks capture spatial structure in environmental data, enhancing species distribution modeling [14], while artificial neural networks improve predictive performance across diverse ecological contexts [15]. In predator-prey systems, continuous-time neural networks can simulate dynamic ecological interactions [16], and training algorithms tailored to predator-prey dynamics help optimize network parameters for modeling complex dynamical behaviors [17].

In this work, we investigate the problem of learning dynamical systems directly from data, with a focus on epidemic and ecological dynamics. Using synthetic datasets generated from canonical ecological and epidemiological models, we evaluate the performance of three data-driven frameworks: Sparse Identification of Nonlinear Dynamics (SINDy), Neural Ordinary Differential Equations (Neural ODEs), and Kolmogorov–Arnold Network ODEs (KANODEs). Numerical experiments demonstrate that these approaches can successfully capture the epidemic, ecological, and coupled behaviors of the systems. SINDy framework offers an interpretable approach by identifying a parsimonious set of active terms in the dynamical system, promoting physical interpretability through sparse regression [18]. In contrast, Neural ODEs provide a flexible, nonparametric framework where the dynamics are represented by a neural network trained to reproduce observed trajectories [19]. KANODEs extend this idea by leveraging the Kolmogorov–Arnold network architecture [20] to efficiently learn dependencies in complex dynamical systems while using a minimal number of parameters [21].

The paper is organized as follows. In Section 2, we introduce the eco-epidemiological modeling framework formulated as a system of ODEs. We begin with a classical epidemic model, then present the predator-prey dynamics, and finally discuss how epidemic processes interact within the predator-prey system. In Section 3, we focus on learning the average dynamics from data using data-driven approaches, including Sparse Identification of Nonlinear Dynamics (SINDy), Kolmogorov–Arnold Network ODEs (KANODEs), and Neural Ordinary Differential Equations (Neural ODE). In Section 4, we consider a spatio-temporal model obtained by incorporating diffusion terms and present a partial learning approach for identifying hidden eco-epidemic coupling mechanisms. The paper ends with conclusions.

2 Ecological and Epidemic Modeling

We begin with classical epidemic models, starting from the Susceptible – Infected – Recovered (SIR) system, which captures the progression of individuals through compartments of infection and recovery, and its simplified variant, the Susceptible–Infected–Susceptible (SIS) model, which accounts for diseases without lasting immunity. Next, we consider the Lotka – Volterra predator-prey system, a cornerstone in mathematical ecology for describing population oscillations arising from predation. Building on this basis, we extend the formulations by constructing a coupled nonlinear eco-epidemiological model that incorporates both population dynamics and infectious disease transmission.

2.1 Epidemic model

The SIR model is the classical epidemic model that assumes that recovery provides permanent immunity and that one cannot be reinfected. This assumption is reasonable for many infectious diseases where immunity is long-lasting or lifelong. The population $u(t)$ is then divided into three compartments: susceptible $u_s(t)$, infected $u_i(t)$, and recovered $u_r(t)$. Each compartment represents the number of individuals in a given state at time t , and the sum of all compartments gives the total population u , which is assumed

constant in the basic SIR setting. The interactions between these compartments determine the dynamics of the epidemic. Susceptible individuals become infected through contact with infected individuals at a rate proportional to both the number of susceptible and infected individuals, while infected individuals recover at a certain rate and become part of the recovered group. The SIR model is described by the following equations

$$\begin{aligned}\frac{du_s}{dt} &= -\sigma u_s u_i, \\ \frac{du_i}{dt} &= \sigma u_s u_i - \omega u_i, \\ \frac{du_r}{dt} &= \omega u_i.\end{aligned}\tag{1}$$

where σ is the infection rate and ω is the recovery rate.

We can simplify the SIR model by assuming that recovered individuals do not acquire permanent immunity but become susceptible after recovery. This is the susceptible–infected–susceptible (SIS) model, which captures the dynamics of diseases where immunity is temporary or absent. Unlike the SIR model, the SIS framework does not include a recovered. Individuals cycle between the susceptible and infected states. The SIS model consists of two nonlinear differential equations that describe the rate of change of the susceptible $u_s(t)$ and infected $u_i(t)$ populations. In this model, susceptible individuals become infected through contact with infected individuals, and infected individuals recover and immediately return to the susceptible compartment, maintaining the potential for reinfection. This is suitable for modeling diseases or infections that occur regularly within a population. The SIS model is described by the following equations

$$\begin{aligned}\frac{du_s}{dt} &= -\sigma u_s u_i + \omega u_i, \\ \frac{du_i}{dt} &= \sigma u_s u_i - \omega u_i,\end{aligned}\tag{2}$$

where σ is the infection rate and ω is the recovery rate.

2.2 Predator-Prey Model

The Lotka–Volterra model provides a mathematical framework for describing the dynamics of predator–prey interactions within ecological systems. It is formulated as a system of two coupled differential equations that capture the temporal evolution of predator and prey populations. A widely studied modification introduces logistic growth for the prey population, leading to a pair of first-order nonlinear differential equations that govern the rates of change of the prey $u(t)$ and predator $v(t)$

$$\begin{aligned}\frac{du}{dt} &= \alpha u \left(1 - \frac{u}{k}\right) - \beta u v \\ \frac{dv}{dt} &= \delta v u - \gamma v\end{aligned}\tag{3}$$

where $u(t)$ denotes the prey population, $v(t)$ denotes the predator population, α is the intrinsic birth rate of the prey, k is the carrying capacity of the environment, β is the predation rate describing how frequently predators consume prey, δ is the predator reproduction rate corresponding to the conversion of consumed prey into predator offspring, and γ is the natural death rate of predators. In formulation 3, the first term in the prey equation represents logistic growth. When resources are abundant, the prey population increases rapidly but slows down as it approaches the carrying capacity. The second term captures the reduction due to predation. To simplify the model and explicitly account for natural mortality of the prey, the logistic term is replaced with a quadratic mortality term ηu^2 , where η represents

density-dependent death processes, including competition and resource limitation. The resulting system takes the form

$$\begin{aligned}\frac{du}{dt} &= \alpha u - \beta u v - \eta u^2, \\ \frac{dv}{dt} &= \delta u v - \gamma v.\end{aligned}\tag{4}$$

This modification removes the explicit dependence on the carrying capacity k and instead assumes that prey mortality grows quadratically with population size. In this way, the self-limiting nature of prey growth is preserved while offering a more flexible representation of mortality mechanisms that may arise from competition, resource depletion, or other density-dependent effects.

2.3 Epidemic Dynamics in the Predator-Prey Model

We consider a combined model that integrates the dynamics of disease into the predator-prey framework by incorporating both susceptible and infected classes for prey and predator populations. The goal of this formulation is to investigate how infection modifies interspecies interactions and influences the stability and long-term behavior of population sizes.

Let u_s denote the susceptible prey population, u_i the infected prey population, v_s the susceptible predator population, and v_i the infected predator population. The temporal evolution of these populations is governed by the following system of differential equations

$$\begin{aligned}\frac{du_s}{dt} &= \alpha_s u_s + \alpha_i u_i - \beta_s^s u_s v_s - \beta_i^s u_s v_i - \gamma_s^u u_s^2 - \sigma_i^s u_s u_i - \sigma_{vi}^s u_s v_i + \omega_i u_i, \\ \frac{du_i}{dt} &= -\beta_s^i u_i v_s - \beta_i^i u_i v_i - \gamma_i^u u_i^2 + \sigma_i^s u_s u_i + \sigma_{vi}^s u_s v_i - \omega_i u_i, \\ \frac{dv_s}{dt} &= -\gamma_s^v v_s + \delta_s^s v_s u_s + \delta_i^s v_s u_i - \sigma_i^{vs} v_s u_i - \sigma_{vi}^{vs} v_s v_i + \omega_{vi} v_i, \\ \frac{dv_i}{dt} &= -\gamma_i^v v_i + \delta_s^i v_i u_s + \delta_i^i v_i u_i + \sigma_i^{vs} v_s u_i + \sigma_{vi}^{vs} v_s v_i - \omega_{vi} v_i,\end{aligned}\tag{5}$$

where α_s is the intrinsic growth rate of susceptible prey, α_i is the intrinsic growth rate of infected prey, β_s^s is the predation rate of susceptible predators on susceptible prey, β_i^s is the predation rate of infected predators on susceptible prey, β_s^i is the predation rate of susceptible predators on infected prey, β_i^i is the predation rate of infected predators on infected prey, γ_s^u is the density-dependent mortality rate of susceptible prey, γ_i^u is the density-dependent mortality rate of infected prey, γ_s^v is the intrinsic mortality rate of susceptible predators, γ_i^v is the intrinsic mortality rate of infected predators, δ_s^s is the reproduction rate of susceptible predators from consuming susceptible prey, δ_i^s is the reproduction rate of susceptible predators from consuming infected prey, δ_s^i is the reproduction rate of infected predators from consuming susceptible prey, δ_i^i is the reproduction rate of infected predators from consuming infected prey, σ_i^s is the rate of disease transmission from infected prey to susceptible prey, σ_{vi}^s is the rate of disease transmission from infected predators to susceptible prey, σ_i^{vs} is the rate of disease transmission from infected prey to susceptible predators, σ_{vi}^{vs} is the rate of disease transmission from infected predators to susceptible predators, ω_i is the rate at which infected prey recover and become susceptible, ω_{vi} is the rate at which infected predators recover and return to the susceptible state.

2.4 Problem Formulation

We express the coupled eco-epidemiological dynamics as a system of ordinary differential equations (ODEs), capturing time evolution in a general and flexible form. To account for spatial heterogeneity and movement of populations, we augment the ODE system with discrete diffusion terms, thereby formulating a spatio-temporal model. This generalization enables us to study not only the temporal evolution of epidemic-ecological interactions but also their spatial spread.

We consider the general ODE system

$$\frac{dy}{dt} = f(y), \quad y(0) = y^0, \quad (6)$$

where $y(t)$ is the state vector and $f(t, y)$ defines the model dynamics. Below are several instances of $f(y)$ used in this work.

- *SIR model*: State vector $y = (u_s, u_i, u_r)^\top$.

$$f_{\text{SIR}}(y) = \begin{pmatrix} -\sigma u_s u_i \\ \sigma u_s u_i - \omega u_i \\ \omega u_i \end{pmatrix}, \quad (7)$$

with $y(0) = (u_{s0}, u_{i0}, u_{r0})^\top$.

- *SIS model*: State vector $y = (u_s, u_i)^\top$.

$$f_{\text{SIS}}(y) = \begin{pmatrix} -\sigma u_s u_i + \omega u_i \\ \sigma u_s u_i - \omega u_i \end{pmatrix},$$

with $y(0) = (u_{s0}, u_{i0})^\top$.

- *Lotka–Volterra (predator–prey)*: State vector $y = (u, v)^\top$ with u = prey, v = predator.

$$f_{\text{LV}}(y) = \begin{pmatrix} \alpha u - \beta u v - \eta u^2 \\ \delta u v - \gamma v \end{pmatrix}, \quad (8)$$

with $y(0) = (u_0, v_0)^\top$. Alternatively, prey mortality can be modeled by $-\eta u^2$ instead of logistic growth.

- *Lotka–Volterra–SIS (eco-epidemiological)*: State vector $y = (u_s, u_i, v_s, v_i)^\top$ with susceptible/infected prey and predator populations.

$$f_{\text{LVSI}}(y) = \begin{pmatrix} \alpha_s u_s + \alpha_i u_i - \beta_s^s u_s v_s - \beta_i^s u_s v_i - \gamma_s^u u_s^2 - \sigma_s^s u_s u_i - \sigma_{vi}^s u_s v_i + \omega_i u_i \\ -\beta_s^i u_i v_s - \beta_i^i u_i v_i - \gamma_i^u u_i^2 + \sigma_i^s u_s u_i + \sigma_{vi}^s u_s v_i - \omega_i u_i \\ -\gamma_s^v v_s + \delta_s^s v_s u_s + \delta_i^s v_s u_i - \sigma_i^{vs} v_s u_i - \sigma_{vi}^{vs} v_s v_i + \omega_{vi} v_i \\ -\gamma_i^v v_i + \delta_s^i v_i u_s + \delta_i^i v_i u_i + \sigma_i^{vs} v_s u_i + \sigma_{vi}^{vs} v_s v_i - \omega_{vi} v_i \end{pmatrix}, \quad (9)$$

with $y(0) = (u_{s0}, u_{i0}, v_{s0}, v_{i0})^\top$.

To numerically solve the time-dependent problem (6) on the interval $0 \leq t \leq T$, time integration is performed using an explicit Runge–Kutta (RK) method. Given a time step τ_n and the numerical solution $y^n \approx y(t^n)$ at time t^n , an s -stage RK method is defined by

$$k_i = f \left(y^n + \tau_n \sum_{j=1}^{i-1} a_{ij} k_j \right), \quad i = 1, \dots, s, \quad (10)$$

$$y^{n+1} = y^n + \tau_n \sum_{i=1}^s b_i k_i. \quad (11)$$

The coefficients $\{a_{ij}, b_i\}$ characterize the specific RK scheme and are typically represented in a Butcher tableau. In this work, we employ an explicit Runge–Kutta method of order 4.

3 Learning Ecological and Epidemic Dynamics

Classical modeling frameworks require explicit knowledge of $f(y)$ in (6). However, in many real-world eco-epidemiological systems, the exact functional form of the dynamics is unknown or too complex to be expressed analytically. We consider several data-driven approaches, including Neural ODEs (NODEs), Kolmogorov–Arnold Network ODEs (KANODEs), and Sparse Identification of Nonlinear Dynamics (SINDy), to learn the underlying dynamics directly from observational data.

Given a set of observed data $\{y^n\}_{i=1}^N$, we define a loss function to quantify the difference between the predicted values and the observations

$$\mathcal{L}(\theta) = \frac{1}{N} \sum_{n=1}^N \|y_\theta^n - y^n\|^2. \quad (12)$$

As observed data, we use the results obtained from the numerical simulations described in the previous section. A fixed time-stepping scheme is employed to generate the time series, to which random noise is added. We then investigate the ability of the considered data-driven approaches to learn the underlying dynamics from these noisy observations.

3.1 Neural Ordinary Differential Equations (NODEs)

The Neural ODEs framework provides a powerful and flexible tool for modeling a wide range of dynamical systems. By using observed data, Neural ODEs can identify hidden system dynamics, predict future scenarios, and assess how ecosystems respond to changing environmental and epidemiological conditions. Neural ODEs transform the classical problem of specifying exact model equations into a data-driven learning problem, where the network approximates the unknown dynamics. This approach can handle complex interactions between ecological and epidemiological components, capturing feedback loops and nonlinear couplings that are difficult to encode manually.

In Neural ODEs, the right-hand side f in (6) is parameterized using a neural network with learnable parameters θ

$$\frac{dy}{dt} \approx \hat{f}_\theta(y) = \text{NN}(y; \theta).$$

The network is provided with the initial condition $y(0) = y^0$, and the predicted trajectory $y_\theta(t)$ is obtained by integrating the neural network over time using a differentiable ODE solver.

Once the Neural ODE is learned, it can be treated exactly the same way as a classical ODE. Standard numerical integration methods, such as Runge–Kutta schemes, are used within the solver, and the integration process is differentiable with respect to the network parameters θ . Neural ODEs employ the same architecture as a standard multilayer perceptron (MLP), composed of several layers of affine transformations and nonlinear activation functions

$$\text{NN}(y; \theta) = W^{(L)} \sigma \left(W^{(L-1)} \sigma \left(\dots \sigma \left(W^{(1)} y + b^{(1)} \right) \dots \right) + b^{(L-1)} \right) + b^{(L)},$$

where $W^{(\ell)}$ and $b^{(\ell)}$ are the weights and biases of the ℓ -th layer, $\sigma(\cdot)$ denotes a nonlinear activation function (e.g., tanh, ReLU, or sigmoid), and $\theta = \{W^{(\ell)}, b^{(\ell)}\}_{\ell=1}^L$ denotes the full set of trainable parameters.

3.2 Kolmogorov–Arnold Network ODEs (KANODEs)

Multilayer perceptrons (MLPs) are a foundational deep learning architecture based on the composition of affine transformations with nonlinear activation functions. Kolmogorov–Arnold Networks (KANs) offer an alternative formulation inspired by the Kolmogorov–Arnold representation theorem [22, 23], in which learnable univariate functions replace fixed pointwise activations. While Neural ODEs typically employ MLPs to parameterize vector fields through matrix multiplications and scalar nonlinearities, KANODEs instead leverage KAN architectures built on adaptive spline representations to approximate the underlying

dynamics [21]. This design promotes interpretability and often achieves comparable expressiveness with fewer trainable parameters. KANODEs transform the problem of identifying the right-hand side of an ODE into learning a composition of flexible nonlinear functions, allowing the model to discover fine-scale structure in ecological or epidemiological processes. Because the nonlinearities along each connection are explicitly represented via splines, KANODEs can provide improved transparency, smoother learned dynamics, and enhanced sample efficiency.

In the KANODEs formulation, the right-hand side f in (6) is parameterized using a KAN with learnable spline coefficients,

$$\frac{dy}{dt} \approx \hat{f}_\theta(y) = \text{KAN}(y; \theta).$$

Given the initial condition $y(0) = y^0$, the predicted trajectory $y_\theta(t)$ is obtained by integrating the KAN-defined vector field using a differentiable ODE solver, exactly as in the Neural ODE framework. KANs are composed of layers of univariate spline functions acting along the connections between nodes. Each layer applies trainable spline transformations to linear combinations of the input variables, enabling flexible and interpretable nonlinear representations. The model parameters θ consist of the spline control points. KANs have attracted considerable interest in recent studies. To alleviate the computational cost associated with B-spline bases, [24] introduces Gaussian radial basis functions (RBFs) as an alternative representation. In [25], the authors propose an adaptive formulation that improves both accuracy and numerical stability. In [26], a Free-RBF-KAN architecture is developed, incorporating adaptive learning grids and trainable smoothness parameters. Moreover, [27] establishes a structural equivalence between KANs and geometrically refined multi-channel MLPs, showing that KAN spline bases provide localized support and act as an implicit preconditioner in the ReLU basis.

Once the KAN-based ODEs are trained, they can be treated as standard ordinary differential equations and integrated using conventional numerical solvers, such as Runge–Kutta methods. Unlike MLP-based Neural ODEs, KANODEs provide a function-level representation of the learned dynamics, offering enhanced expressiveness in low-data regimes and improved interpretability of ecological and epidemiological feedback mechanisms.

3.3 Sparse Identification of Nonlinear Dynamics (SINDy)

Sparse Identification of Nonlinear Dynamics [18, 28] is a data-driven method for discovering governing equations of dynamical systems directly from observational data. Unlike black-box neural networks, SINDy seeks a parsimonious representation of the dynamics by identifying a small subset of functions from a predefined library that accurately describes the system.

Formally, given observed data, SINDy assumes the dynamics can be written as

$$\frac{dy}{dt} \approx f_\Xi(y) = \Theta(y)\Xi,$$

where $\Theta(y)$ is a library of candidate functions (e.g., polynomials, trigonometric functions, interaction terms), and Ξ is a sparse coefficient matrix to be learned. Sparsity in the SINDy framework is typically enforced using techniques such as Sequential Thresholded Least Squares (STLSQ) or LASSO regression, which promote models that are parsimonious, interpretable, and consistent with the underlying physical principles [18, 29]. However, when the data are contaminated with noise, numerical differentiation can amplify errors, resulting in spurious or unstable terms in the identified equations. To alleviate these effects, regularization strategies are incorporated into the sparse regression step. For instance, ridge regularization (L_2 penalty) can be introduced to stabilize coefficient estimation and enhance robustness to noisy measurements. Moreover, depending on the noise level in the dataset, it may also be necessary to filter data prior to solving for the sparse coefficient matrix Ξ . For example, total variation (TV) regularization can be used to denoise the data and improve the stability and accuracy of the sparse regression procedure [30]. In addition, Neural ODEs may be employed as a data pre-processing tool to obtain smoothed trajectories, particularly when the data are irregularly sampled in time. Neural ODEs naturally operate in continuous time, thereby eliminating the need for uniform temporal discretization. Once

the smooth continuous dynamics have been learned, the SINDy framework can be applied subsequently to extract an interpretable and parsimonious representation of the underlying governing equations.

SINDy produces explicit, symbolic forms of the governing equations, which allows domain scientists to interpret and validate the model; it can reveal dominant interactions and nonlinearities; and it is computationally efficient for moderate-dimensional systems. However, SINDy relies on the choice of the function library $\Theta(y)$, and its performance may degrade when the system dynamics are highly complex, noisy, or involve functions outside the predefined library. SINDy is particularly well-suited for systems where the underlying mechanisms are partially known, and interpretability is a priority.

4 Learning Hidden Local Eco-Epidemic Coupling

Finally, we present an extension of the proposed learning approach to infer hidden local eco-epidemic coupling. We consider a spatio-temporal model by incorporating diffusion operators in one- and two-dimensional formulations. A finite difference method is applied to construct a discrete time-dependent system. We then propose a partial learning strategy in which the diffusion/transport processes are assumed to be known, while the hidden local eco-epidemic coupling is learned from solution data defined on a spatial grid. The applicability of the approach is demonstrated using Neural ODEs.

4.1 Spatio-Temporal Model with Finite Difference Diffusion

To model diffusion in one or two spatial dimensions and discretize using the finite difference method. For a one-dimensional (1D) domain of length X discretized into N_x points with spacing $\Delta x = X/(N_x - 1)$, the diffusion term

$$\nabla(\kappa \nabla y) = \frac{\partial}{\partial x} \left(\kappa \frac{\partial y}{\partial x} \right)$$

at interior points is approximated by the standard central difference

$$\frac{\partial}{\partial x} \left(\kappa \frac{\partial y}{\partial x} \right) \Big|_{x_i} \approx \frac{\kappa_{i+1/2}(y_{i+1} - y_i) - \kappa_{i-1/2}(y_i - y_{i-1})}{\Delta x^2}, \quad i = 1, \dots, N_x - 2,$$

where $\kappa_{i\pm1/2}$ denotes the diffusion coefficient at cell interfaces. Zero Neumann boundary conditions, corresponding to no-flux boundaries,

$$\frac{\partial y}{\partial x} \Big|_{x=0} = 0, \quad \frac{\partial y}{\partial x} \Big|_{x=X} = 0,$$

are imposed by enforcing

$$y_1 - y_0 = 0, \quad y_{N_x-1} - y_{N_x-2} = 0,$$

which leads to the modified finite-difference approximations at the boundary points

$$\frac{\partial}{\partial x} \left(\kappa \frac{\partial y}{\partial x} \right) \Big|_{x_0} \approx \frac{2\kappa_{1/2}(y_1 - y_0)}{\Delta x^2}, \quad \frac{\partial}{\partial x} \left(\kappa \frac{\partial y}{\partial x} \right) \Big|_{x_{N_x-1}} \approx \frac{2\kappa_{N_x-3/2}(y_{N_x-2} - y_{N_x-1})}{\Delta x^2}.$$

For a two-dimensional rectangular domain of size $L_x \times L_y$ discretized into $N_x \times N_y$ grid points

$$\nabla(\kappa \nabla y) = \frac{\partial}{\partial x_1} \left(\kappa \frac{\partial y}{\partial x_1} \right) + \frac{\partial}{\partial x_2} \left(\kappa \frac{\partial y}{\partial x_2} \right), \quad x = (x_1, x_2),$$

the discrete Laplacian at interior nodes (i, j) is approximated by

$$\begin{aligned} \frac{\partial}{\partial x_1} \left(\kappa \frac{\partial y}{\partial x_1} \right) \Big|_{x_{ij}} &\approx \frac{\kappa_{i+1/2,j}(y_{i+1,j} - y_{i,j}) - \kappa_{i-1/2,j}(y_{i,j} - y_{i-1,j})}{\Delta x_1^2}, \\ \frac{\partial}{\partial x_2} \left(\kappa \frac{\partial y}{\partial x_2} \right) \Big|_{x_{ij}} &\approx \frac{\kappa_{i,j+1/2}(y_{i,j+1} - y_{i,j}) - \kappa_{i,j-1/2}(y_{i,j} - y_{i,j-1})}{\Delta x_2^2}, \end{aligned}$$

where (i, j) denotes the grid point in the 2D mesh with $x_{ij} = (x_{1,i}, x_{2,j})$, and $\kappa_{i\pm 1/2,j}$, $\kappa_{i,j\pm 1/2}$ are the diffusion coefficients at the cell interfaces in x_1 and x_2 directions, respectively.

Including diffusion, the spatially discretized system (6) can be written as

$$\frac{dy}{dt} = Ly + f(y), \quad (13)$$

where $y(t) \in \mathbb{R}^{M \times N}$ denotes the state vector collecting all M components at N spatial grid points ($N = N_x$ in 1D and $N = N_x \times N_y$ in 2D), L is the discrete Laplacian obtained from a finite difference discretization, and $f(y)$ represents the local reaction term. We note that in some cases, cross-diffusion terms can be incorporated to account for interactions between components. In this case, we assume no cross-diffusion between components, so the resulting discrete Laplacian matrix L has a block-diagonal structure, with each block corresponding to the diffusion of a single component. The resulting system of ODEs (13) can be integrated using the standard time-stepping schemes described above. In this work, we consider systems with very small diffusion and employ explicit time-stepping schemes for temporal integration.

4.2 Learning Hidden Local Coupling

We now describe the learning strategy used to identify unknown local reaction coupling in the spatio-temporal model. Our primary focus is on learning the local reaction term, rather than fully resolving the coupled spatio-temporal behavior. Accordingly, we assume that the diffusion structure, or spatial connectivity, is known and fixed. Based on this assumption, we propose a partial learning framework that aims to identify hidden local interactions among the components of the system. This strategy enables us to infer the essential dynamics while leveraging prior knowledge of the spatial diffusion operator, thereby reducing the complexity of the learning problem and improving interpretability. Moreover, by concentrating on the local coupling terms, the proposed approach is able to capture subtle interactions that may be overlooked by fully data-driven models.

In this framework, the diffusion operator in (13) is explicitly incorporated into the model and treated as fixed, while the reaction term $f(y)$ is approximated by a neural network. This separation allows the learning process to focus exclusively on the unknown local nonlinear coupling between components, further reducing model complexity and enhancing interpretability. The resulting system is formulated as follows

$$\frac{dy}{dt} = Ly + \hat{f}_\theta(y),$$

where L denotes the known discrete Laplacian, and \hat{f}_θ is a neural network parameterized by θ .

In the training process, the spatio-temporal solution data are normalized using a global mean and standard deviation computed over all time steps and spatial locations. The training strategy explicitly separates the known diffusion dynamics from the unknown reaction processes, allowing the learning algorithm to focus on identifying the local nonlinear coupling between system components. By fixing the diffusion operator and learning only the reaction term, the dimensionality of the learning problem is significantly reduced, leading to improved numerical stability and interpretability. Moreover, the use of short temporal windows mitigates error accumulation during time integration and enables robust training even for long-time simulations. Since the diffusion term is treated deterministically and applied component-wise using a preassembled Laplacian matrix, the resulting NODEs preserve the underlying physical structure of the spatio-temporal model while benefiting from the flexibility of neural network-based closures.

5 Numerical Experiments

We consider three datasets generated by numerically solving the ODE system (6) using the right-hand sides f_{SIR} in (7), f_{LV} in (8), and the coupled model f_{LVSIS} in (9). The SINDy framework is implemented

using the PySINDy library [28], while the machine learning models are trained using PyTorch [31], which provides automatic differentiation and flexible tools for optimizing neural network representations of the underlying dynamics. The SIR, LV, and LVSIS systems are integrated over a fixed time interval with prescribed initial conditions to obtain the reference trajectories.

- *SIR*: The *SIR model* has state vector is $y = (u_s, u_i, u_r)^\top$, with dynamics governed by (7), parameters $\sigma = 0.5$ and $\omega = 0.1$, and initial condition $y(0) = [0.99, 0.01, 0.0]^\top$.
- *LV*: The *Lotka–Volterra (predator–prey) model* has state vector $y = (u, v)^\top$, representing prey (u) and predator (v) populations. Its dynamics follow (8) with parameters $\alpha = 0.5$, $\beta = 0.8$, $\delta = 0.4$, $\gamma = 0.3$, initial condition $y(0) = [0.5, 0.5]^\top$, and a small prey mortality $\eta = 0.05$.
- *LVSIS*: The *Lotka–Volterra–SIS (eco-epidemiological) model* has state vector $y = (u_s, u_i, v_s, v_i)^\top$ and dynamics given by (9). The initial condition is $y(0) = [0.7, 0.3, 0.6, 0.4]^\top$. Prey birth rates are set to $\alpha_s = 0.04$ and $\alpha_i = 0.02$, and prey and predator death rates are $\gamma_s^u = \gamma_i^u = 0.02$ and $\gamma_s^v = \gamma_i^v = 0.01$, respectively. Coupling parameters for predator–prey interactions are $\beta_s^s = \beta_s^i = \beta_i^s = \beta_i^i = 0.02$, and for cross-species interactions $\delta_s^s = \delta_s^i = \delta_i^s = \delta_i^i = 0.04$. Transmission and recovery rates are $\sigma_i^s = \sigma_{vi}^s = \sigma_{si}^v = \sigma_{vi}^v = 0.01$ and $\omega_i = \omega_{vi} = 0.01$.

We begin simulations at $t = 0$ and evolve the system up to T_{\max} , with $T_{\max} = 60, 180$, and 1971 for the SIR, LV, and LVSIS datasets, corresponding to the right-hand sides f_{SIR} in (7), f_{LV} in (8), and f_{LVSIS} in (9), respectively. Each simulation is discretized into $N_t = 300$ time steps, producing a dataset that is subsequently split into training and testing subsets. We consider three training proportions $p = 1/3, 1/2$, and $2/3$, corresponding to the first $N = 100, 150$, and 200 time steps. The resulting time series \tilde{Y} , consisting of N points, serves as input for the data-driven discovery methods, including Neural ODEs, KANODEs, and SINDy. The ODE systems in (6) are numerically solved using the SciPy library [32].

We consider the performance of three techniques to learn ecological and epidemic dynamics based on the given dataset. We compare KANODEs and NODEs models across the SIR, LV, and LVSIS datasets. For the KAN architecture, the number of trainable parameters is 360 for the SIR dataset, 160 for the LV dataset, and 640 for the LVSIS dataset ($N_{\text{comp}} - 5 - N_{\text{comp}}$). For NODE₁, the parameter counts are 4,611 for the SIR, 4,482 for the LV, and 4,740 for the LVSIS ($N_{\text{comp}}-64-N_{\text{comp}}$). For NODE₂, the models have 33,539 parameters for SIR, 33,410 for LV, and 33,668 for LVSIS, with a deeper architecture ($N_{\text{comp}}-64-128-128-64-N_{\text{comp}}$). All machine learning models are trained for 500 iterations using the tanh activation function in NODEs.

The prediction accuracy is quantified using relative ℓ^2 errors expressed as percentages. At selected time indices $i \in \mathcal{I}$, the pointwise error is computed as

$$e^n = \frac{\|y_{\text{pred}}^n - y^n\|_2}{\|y^n\|_2} \times 100\%,$$

In addition, we report relative ℓ^2 errors on the training subset and on the full dataset

$$e_{\text{Train}} = \frac{\left(\sum_{n=1}^N \|y_\theta^n - y^n\|^2 \right)^{1/2}}{\left(\sum_{n=1}^N \|y^n\|^2 \right)^{1/2}} \times 100\%, \quad e_{\text{Full}} = \frac{\left(\sum_{n=1}^{N_t} \|y_\theta^n - y^n\|^2 \right)^{1/2}}{\left(\sum_{n=1}^{N_t} \|y^n\|^2 \right)^{1/2}} \times 100\%.$$

5.1 Learning Ecological and Epidemic Dynamics

Figures 1, 2, and 3 show the prediction performance of the three approaches on the SIR, LV, and LVSIS datasets. Results are presented for three training proportions, $p = 1/3, 1/2$, and $2/3$, corresponding to training set sizes $N = p N_t$. The datasets are generated from the original systems without added noise. Additionally, each plot displays the relative ℓ_2 error at several time points (e^n).

The first row of Figures 1, 2, and 3 presents the results obtained using the SINDy framework. On the SINDy framework, we used a second-degree polynomial library and the Sequential Thresholded Least

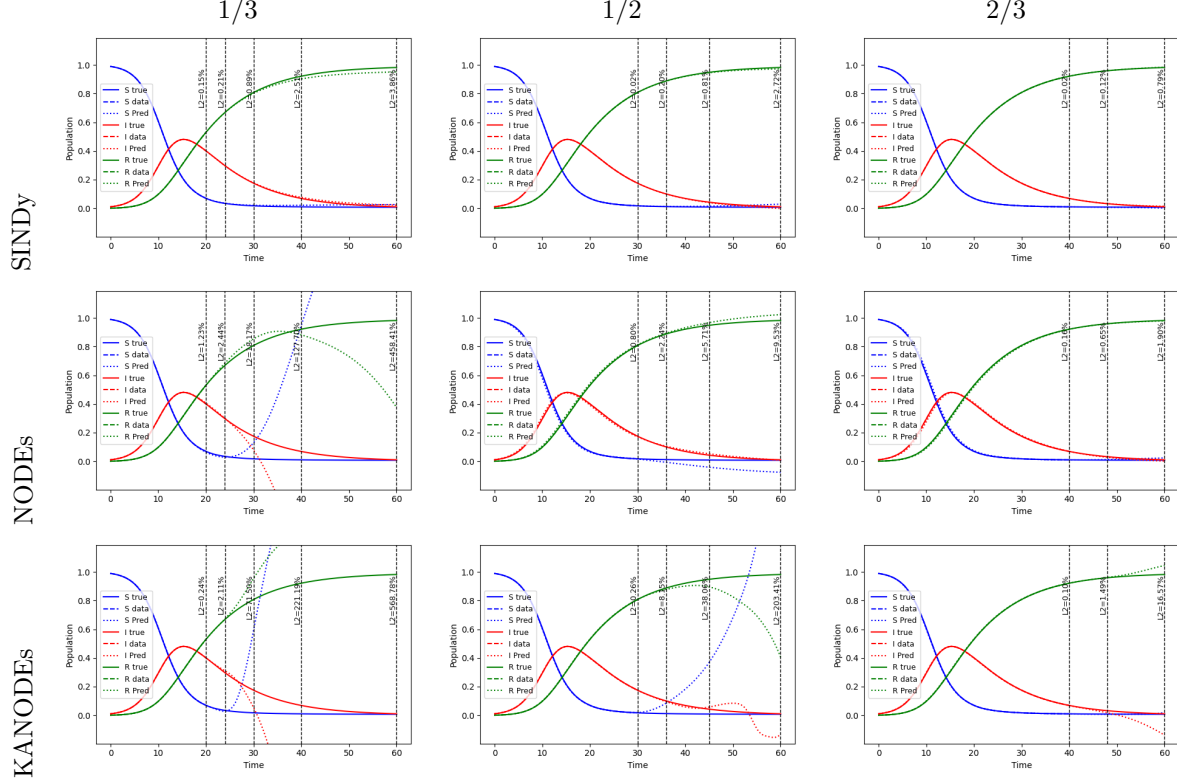


Figure 1: SIR: Comparison of prediction performance

		Learned Equations
1/3	$u'_s = -0.065 - 0.104u_s - 0.001u_i + 0.040u_r + 0.169u_s^2 - 0.198u_su_i - 0.075u_su_r + 0.116u_i^2 + 0.081u_iu_r + 0.034u_r^2$	$u'_i = 0.024 + 0.087u_s + 0.016u_i - 0.079u_r - 0.112u_s^2 + 0.245u_su_i - 0.047u_su_r - 0.141u_i^2 - 0.088u_iu_r + 0.055u_r^2$
$u'_r = 0.041 + 0.017u_s - 0.016u_i + 0.039u_r - 0.057u_s^2 - 0.048u_su_i + 0.122u_su_r + 0.025u_i^2 + 0.007u_iu_r - 0.089u_r^2$	$u'_s = -0.046 - 0.068u_s - 0.078u_i + 0.100u_r + 0.115u_s^2 - 0.268u_su_i + 0.085u_su_r + 0.123u_i^2 + 0.067u_iu_r - 0.052u_r^2$	$u'_i = 0.019 + 0.076u_s + 0.039u_i - 0.096u_r - 0.096u_s^2 + 0.266u_su_i - 0.094u_su_r - 0.148u_i^2 - 0.079u_iu_r + 0.077u_r^2$
$u'_r = 0.027 - 0.008u_s + 0.039u_i - 0.004u_r - 0.019u_s^2 + 0.002u_su_i + 0.009u_su_r + 0.025u_i^2 + 0.012u_iu_r - 0.024u_r^2$	$u'_s = -0.040 - 0.056u_s - 0.105u_i + 0.121u_r + 0.096u_s^2 - 0.292u_su_i + 0.141u_su_r + 0.125u_i^2 + 0.062u_iu_r - 0.082u_r^2$	$u'_i = 0.016 + 0.070u_s + 0.053u_i - 0.107u_r - 0.086u_s^2 + 0.278u_su_i - 0.122u_su_r - 0.149u_i^2 - 0.076u_iu_r + 0.092u_r^2$
$u'_r = 0.024 - 0.014u_s + 0.052u_i - 0.014u_r - 0.010u_s^2 + 0.014u_su_i - 0.019u_su_r + 0.023u_i^2 + 0.014u_iu_r - 0.010u_r^2$	Original Equations	
	$u'_s = -0.5u_su_i$	$u'_i = -0.1u_i + 0.5u_su_i$
	$u'_r = 0.1u_i$	

Table 1: SIR: Learned SINDy equations for different training proportions

Squares (STLSQ) method with a 0.001 threshold. We note that polynomial functions are widely used in applied mathematical modeling, particularly in population dynamics, ecology, and epidemiology [33]. The identified ODEs for each model for different training proportions are presented in Tables 1, 2, and 3. For the SIR model, the learned polynomial terms capture the infection and recovery dynamics. As the training set increases from 1/3 to 2/3, the coefficients approach the true parameters, improving accuracy and stability. In the LV system, the learned equations reproduce the characteristic predator-prey oscillations. The bilinear interaction uv is consistently identified, while quadratic terms u^2 and v^2 provide small corrections for nonlinear effects. Larger training sets improve the match to reference trajectories,

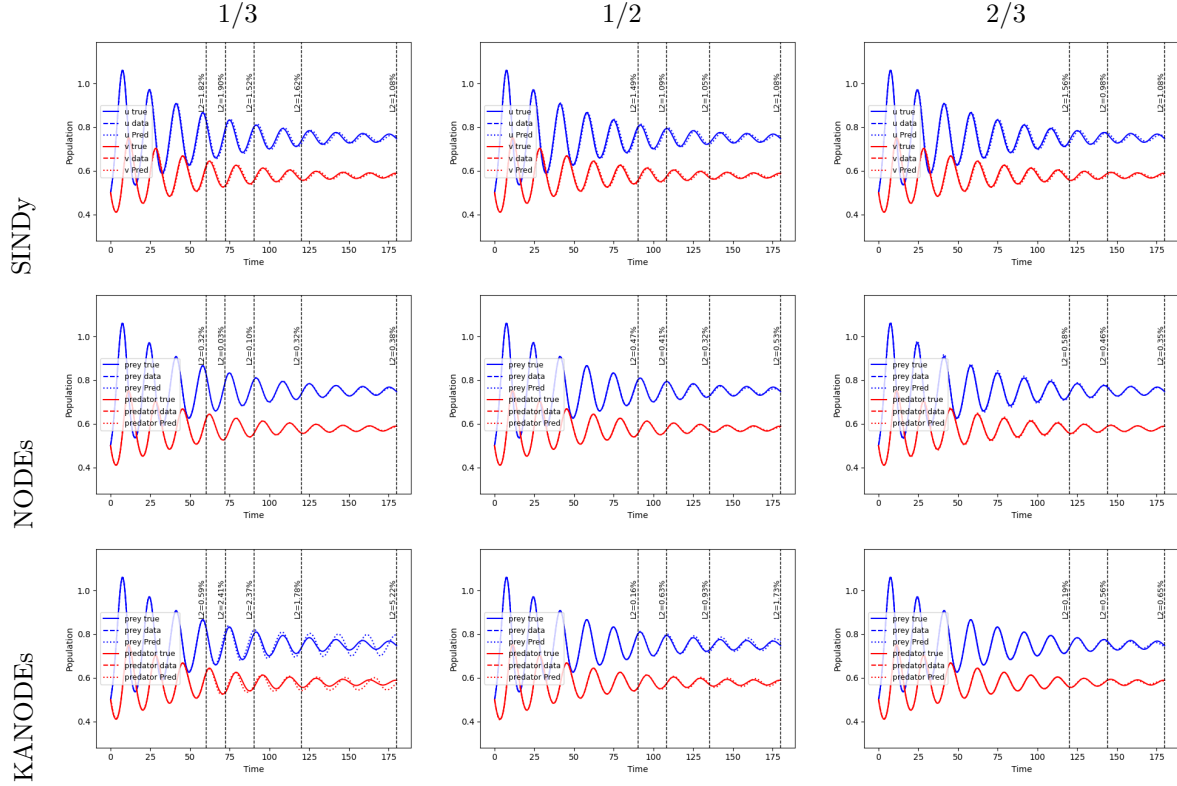


Figure 2: LV: Comparison of prediction performance

	Learned Equations
1/3	$u' = 0.002 + 0.472u + 0.028v - 0.043u^2 - 0.769uv - 0.043v^2$ $v' = -0.001 + 0.017u - 0.320v - 0.007u^2 + 0.386uv + 0.028v^2$
1/2	$u' = 0.001 + 0.472u + 0.031v - 0.043u^2 - 0.769uv - 0.046v^2$ $v' = 0.017u - 0.322v - 0.006u^2 + 0.386uv + 0.030v^2$
2/3	$u' = 0.002 + 0.471u + 0.029v - 0.042u^2 - 0.769uv - 0.045v^2$ $v' = 0.017u - 0.322v - 0.006u^2 + 0.386uv + 0.030v^2$
Original Equations	
	$u' = 0.5u - 0.05u^2 - 0.8uv$ $v' = -0.3v + 0.4uv$

Table 2: LV: Learned SINDy equations for different training proportions

particularly in amplitude and period. For the LVSIS eco-epidemiological model, SINDy recovers both intra- and inter-species interactions, including bilinear transmission and predation terms and nonlinear density-dependent effects. Even small training sets capture the qualitative dynamics, while larger sets yield more accurate coefficients and closer agreement with reference trajectories. Overall, we observe that the SINDy framework is capable of capturing the essential structure of the underlying dynamics across all three systems.

In the second and third rows of Figures 1, 2, and 3, we present the results obtained using the two neural network approaches, NODEs and KANODEs. Both methods achieve a good performance, providing accurate reconstructions of the underlying trajectories and demonstrating robust predictive capabilities, particularly with larger training datasets. Increasing the amount of training data consistently enhances prediction accuracy for all methods over all datasets. However, for the SIR dataset, the model exhibits reduced accuracy when predicting beyond the training set. For the more complex oscillatory dynamics of

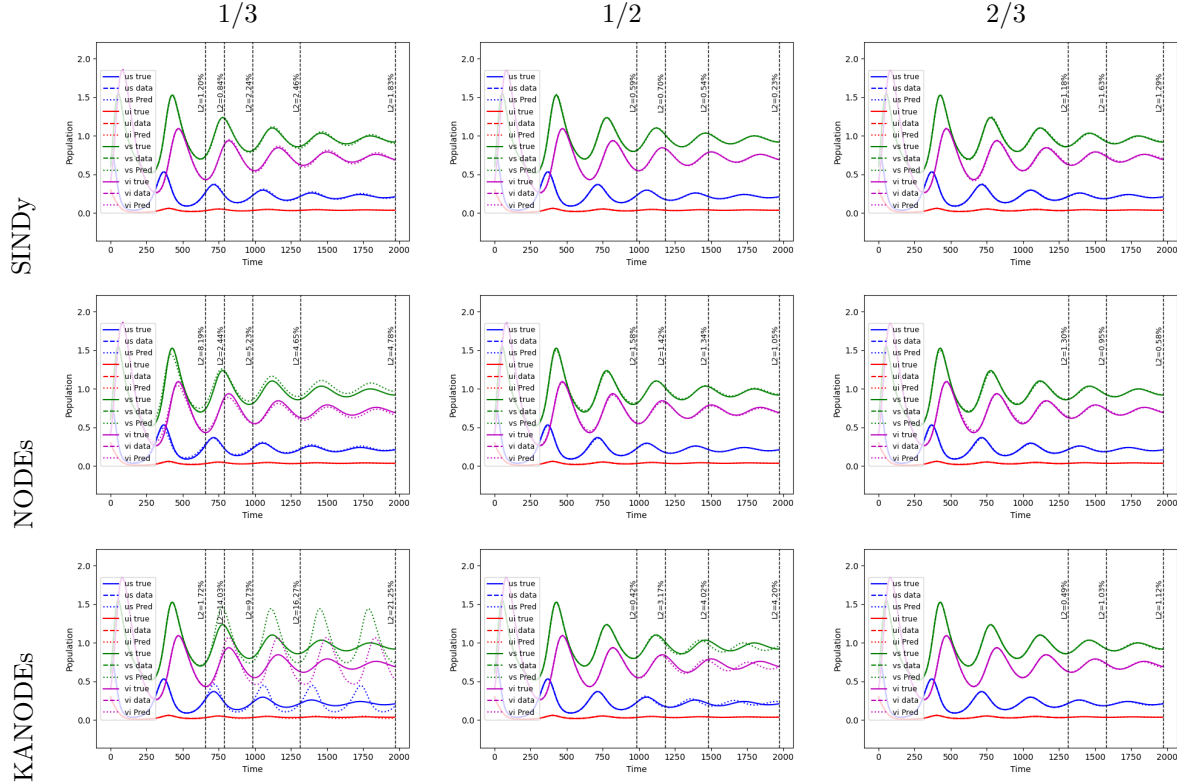


Figure 3: LVSIS: Comparison of prediction performance

the LV and LVSIS models, the models achieve good predictive performance. KANODEs perform well on larger datasets ($p = 2/3$). Neural ODEs yield better extrapolation outside the training set for all models. In the Lotka–Volterra system, both methods achieve good performance across all training proportions, reflecting the richer dynamics. For the LVSIS model, good results are observed for NODEs with $p = 1/2$ and for KANODEs with $p = 2/3$. We note that, for Neural ODEs, we present results using a larger network (NODEs₂), which contains significantly more parameters than KANODEs.

Next, to emulate measurement uncertainty and evaluate the robustness of the models, we generate noisy datasets by perturbing the reference trajectories with additive Gaussian noise

$$\tilde{Y} = Y + \mathcal{N}(0, \sigma^2), \quad Y = \{y(t_i)\}_{i=1}^N, \quad (14)$$

where $\sigma = 0.01$ denotes the standard deviation of the noise, and Y represents the observed noise-free data. It is well known that SINDy is highly sensitive to noise in the training data, often requiring pre-filtering or smoothing techniques to ensure stable recovery of the governing equations. Accordingly, we restrict our noisy-data experiments to the Neural ODE (NODEs₂) and KANODEs frameworks. In Figures 4, 5, and 6, we present the results obtained using the neural network approaches. The SIR model, which exhibits relatively simple dynamics, is highly sensitive to the size of the training set. However, Neural ODEs provide accurate predictions when trained with sufficient temporal information, particularly for $p = 2/3$. The richer and more oscillatory trajectories in the LV dataset allow the models to effectively learn the underlying dynamics, even from smaller training sets. We observe that Neural ODEs generally outperform KANODEs, especially when trained on limited data, by better capturing nonlinear interactions and coupled oscillatory behavior among the species. Overall, both approaches achieve low prediction error when provided with representative training data that adequately characterizes the dynamics of the underlying system.

Learned Equations	
1/3	$u'_s = 0.040u_s + 0.025u_i - 0.001v_i - 0.021u_s^2 - 0.015u_sv_i - 0.019u_sv_s - 0.029u_sv_i + 0.023u_i^2 + 0.014u_iv_s - 0.016u_iv_i - 0.001v_s^2 + 0.002v_sv_i$ $u'_i = -0.009u_i + 0.004u_sv_i + 0.009u_sv_i - 0.014u_i^2 - 0.016u_iv_s - 0.022u_iv_i$ $v'_s = -0.001u_s + 0.081u_i - 0.012v_s + 0.011v_i + 0.006u_s^2 - 0.075u_sv_i + 0.040u_sv_s - 0.018u_sv_i - 0.118u_i^2 + 0.061u_iv_s + 0.001v_s^2 - 0.011v_sv_i$ $v'_i = -0.004u_i - 0.020v_i - 0.001u_s^2 + 0.020u_sv_i + 0.040u_sv_i - 0.019u_i^2 - 0.003u_iv_s + 0.049u_iv_i + 0.010v_sv_i$
1/2	$u'_s = 0.040u_s + 0.038u_i + 0.001v_s - 0.001v_i - 0.020u_s^2 - 0.029u_sv_i - 0.018u_sv_s - 0.035u_sv_i + 0.028u_iv_s - 0.017u_iv_i - 0.001v_s^2 + 0.002v_sv_i$ $u'_i = -0.008u_i + 0.004u_sv_i + 0.009u_sv_i - 0.015u_i^2 - 0.016u_iv_s - 0.023u_iv_i$ $v'_s = 0.001u_s - 0.031u_i - 0.012v_s + 0.011v_i + 0.001u_s^2 + 0.031u_sv_i + 0.036u_sv_s + 0.015u_sv_i + 0.066u_i^2 - 0.034u_iv_s + 0.039u_iv_i + 0.004v_s^2 - 0.014v_sv_i + 0.001v_i^2$ $v'_i = 0.013u_i - 0.020v_i + 0.006u_sv_i + 0.001u_sv_i + 0.037u_sv_i - 0.045u_i^2 + 0.008u_iv_s + 0.040u_iv_i + 0.010v_sv_i$
2/3	$u'_s = 0.040u_s + 0.038u_i + 0.001v_s - 0.001v_i - 0.020u_s^2 - 0.029u_sv_i - 0.018u_sv_s - 0.035u_sv_i + 0.026u_iv_s - 0.017u_iv_i - 0.001v_s^2 + 0.001v_sv_i$ $u'_i = -0.008u_i + 0.004u_sv_i + 0.009u_sv_i - 0.015u_i^2 - 0.016u_iv_s - 0.023u_iv_i$ $v'_s = 0.001u_s - 0.032u_i - 0.011v_s + 0.011v_i + 0.001u_s^2 + 0.032u_sv_i + 0.036u_sv_s + 0.015u_sv_i + 0.069u_i^2 - 0.032u_iv_s + 0.039u_iv_i + 0.003v_s^2 - 0.014v_sv_i + 0.001v_i^2$ $v'_i = 0.012u_i - 0.020v_i + 0.007u_sv_i + 0.001u_sv_i + 0.037u_sv_i - 0.044u_i^2 + 0.008u_iv_s + 0.041u_iv_i + 0.010v_sv_i$
	Original Equations
	$u'_s = 0.04u_s + 0.03u_i - 0.01u_s^2 - 0.01u_sv_i - 0.02u_sv_s - 0.03u_sv_i$ $u'_i = -0.01u_i + 0.01u_sv_i + 0.01u_sv_i - 0.01u_i^2 - 0.02u_iv_s - 0.02u_iv_i$ $v'_s = -0.01v_s + 0.01v_i + 0.04u_sv_s + 0.03u_iv_s - 0.01v_sv_i$ $v'_i = -0.02v_i + 0.04u_sv_i + 0.01u_iv_s + 0.041u_iv_i + 0.01v_sv_i$

Table 3: LVSIS: Learned SINDy equations for different training proportions

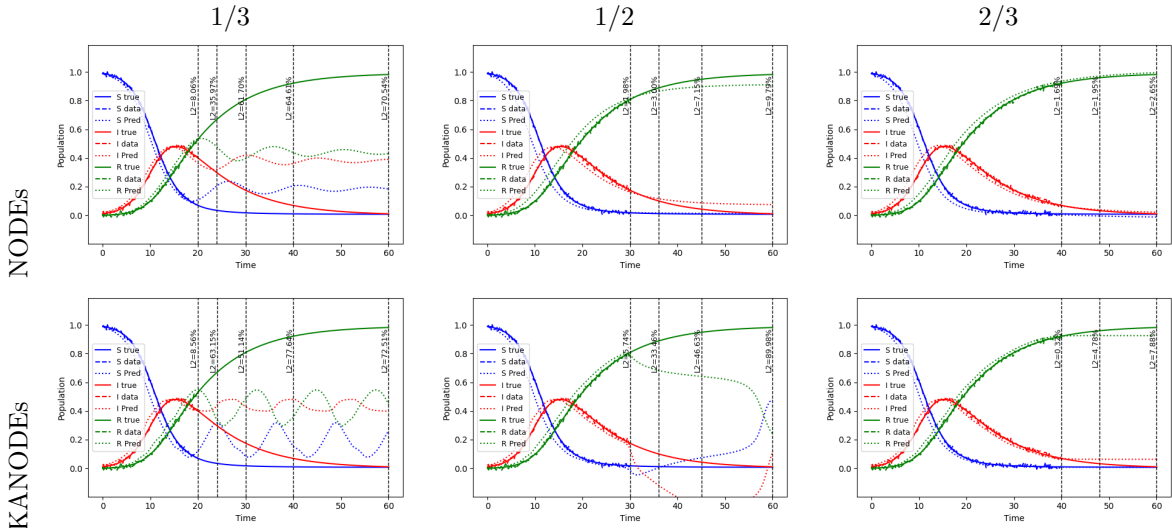


Figure 4: SIR: Comparison of prediction performance. Noised data

In Table 4, we present the relative ℓ^2 errors (in percent) on the training subset and on the full time horizon for the SIR, LV, and LVSIS datasets, using both original and noised data. For the original (noise-free) data, SINDy achieves consistently low training and full errors across all systems, reflecting its effectiveness when the governing dynamics are sparse and the data are clean. In contrast, NODEs models exhibit small training errors but, in several cases, significantly larger full-horizon errors, particularly for the SIR system at shorter training horizons, indicating sensitivity to extrapolation beyond the observed

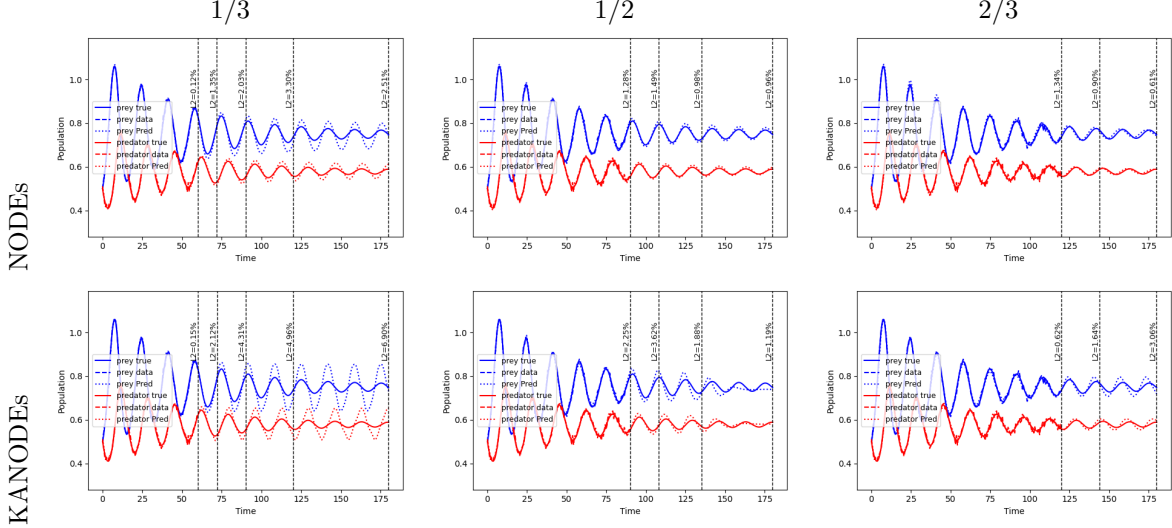


Figure 5: LV: Comparison of prediction performance. Noised data

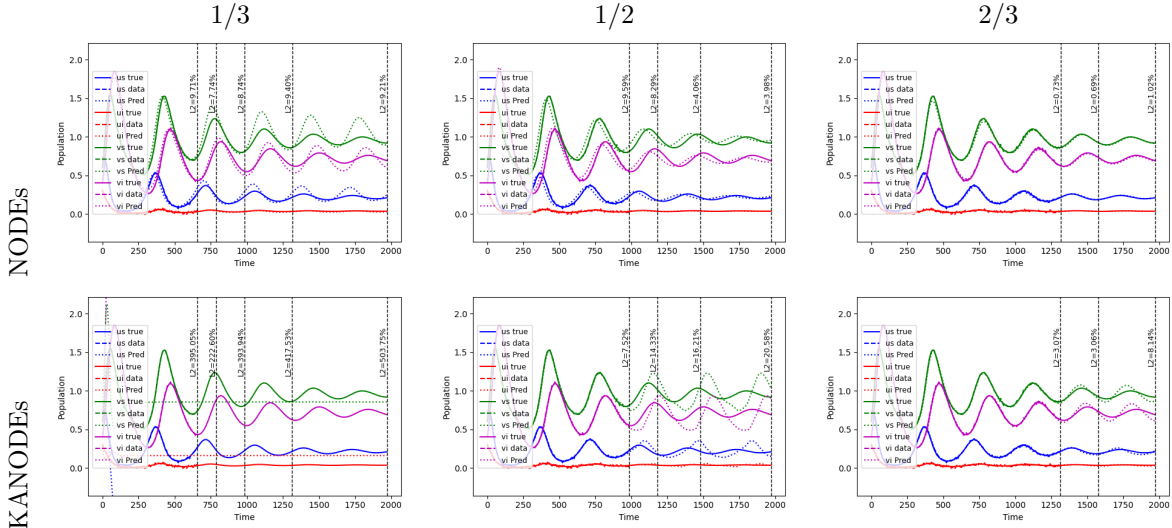


Figure 6: LVSIS: Comparison of prediction performance. Noised data

time window. Increasing model capacity from NODE₁ to NODE₂ generally improves full-horizon accuracy, especially for longer training fractions. For the LV system, all neural models demonstrate stable performance on the original data, with comparable training and full errors, suggesting that the dynamics are well captured even with limited observations. For the more complex LVSIS system, deeper NODEs architectures reduce both training and full errors relative to shallow models, while KANODEs achieve the smallest training errors for longer training horizons, albeit with occasional degradation in long-time prediction accuracy. When trained on noisy data, SINDy fails to produce stable models, while neural approaches remain viable. However, noise significantly impacts extrapolation accuracy, particularly for shallow NODEs and KANODEs at short training horizons. Overall, the results highlight a trade-off between model expressiveness, robustness to noise, and long-time predictive accuracy, with deeper NODEs providing the most consistent performance across all test cases.

	Original data						Noised data					
	1/3		1/2		2/3		1/3		1/2		2/3	
	Train	Full	Train	Full	Train	Full	Train	Full	Train	Full	Train	Full
SIR												
SINDy	0.06	2.34	0.08	1.01	0.07	0.22	-	-	-	-	-	-
NODEs ₁	1.72	972.0	2.13	10.55	3.16	2.67	10.73	44.72	14.43	11.01	8.27	6.33
NODEs ₂	0.44	186.5	2.43	5.08	1.95	1.64	7.49	53.67	13.18	9.99	9.99	7.72
KANODEs	0.34	259.1	0.49	65.82	0.53	4.30	11.01	57.75	10.29	37.78	7.27	6.59
LV												
SINDy	1.33	1.39	1.46	1.37	1.45	1.35	-	-	-	-	-	-
NODEs ₁	0.37	0.32	0.18	0.31	0.45	0.41	10.73	44.72	14.43	11.01	8.27	6.33
NODEs ₂	0.34	0.28	0.34	0.42	0.62	0.55	0.87	2.55	0.89	0.98	1.12	1.09
KANODEs	0.50	2.10	0.17	0.69	0.29	0.39	11.01	57.75	10.29	37.78	7.27	6.59
LVSIS												
SINDy	0.57	1.16	0.74	0.76	0.74	0.71	-	-	-	-	-	-
NODEs ₁	15.03	20.56	13.98	15.23	10.77	10.28	7.92	17.34	6.13	5.17	8.40	8.04
NODEs ₂	4.66	4.99	1.55	1.40	1.54	1.35	6.29	10.31	8.88	7.82	2.29	2.01
KANODEs	0.42	15.49	0.38	3.33	0.36	0.60	205.9	319.7	1.50	12.32	1.40	3.11

Table 4: Relative errors of trained models in %. Original and noised data

5.2 Learning Hidden Local Coupling in Spatio-Temporal Systems

Finally, we consider the spatio-temporal dynamics of the LVSIS model. Figure 7 presents the reference solutions in one and two spatial dimensions (1D and 2D). Our objective is to learn the local coupling induced by the LVSIS reaction terms, assuming the diffusion process is known. The diffusion is taken to be homogeneous, with diffusion coefficient $\kappa = 10^{-5}$ for each component, and is discretized using a finite difference method on uniform grids consisting of 10 nodes in the 1D case and 7×7 nodes in the 2D case. We consider the semi-discrete system (13) on the spatial domain $[0, 10]^d$, for $d = 1, 2$. The parameters in the reaction term f_{LVSIS} are chosen to be consistent with those used in the previous experiments.

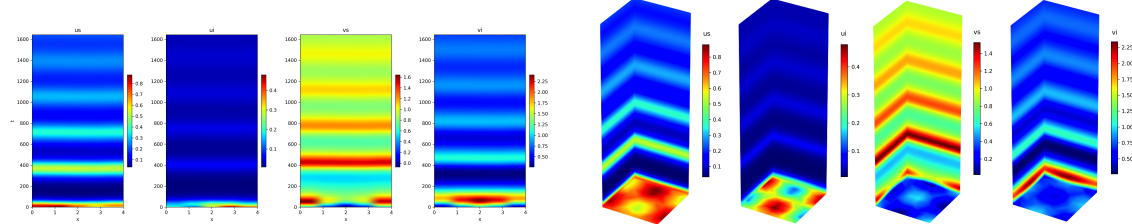


Figure 7: LVSIS: Reference solution. Spatio-temporal model (left: 1D, right: 2D).

	1/3		1/2		2/3	
	Train	Full	Train	Full	Train	Full
	LVSIS					
1D	1.035	9.118	3.668	4.036	1.572	1.485
2D	1.904	8.509	1.499	2.167	1.997	1.856

Table 5: Relative errors of trained model in %. Spatio-temporal model (1D and 2D)

Table 5 reports the relative prediction errors evaluated for different fractions of the training horizon ($p = 1/3, 1/2, 2/3$). In both cases, the trained NODEs₂ model achieves low training errors and maintains good generalization to the full prediction interval, with performance improving as the available training

Dynamics
Prediction

1/3

1/2

2/3

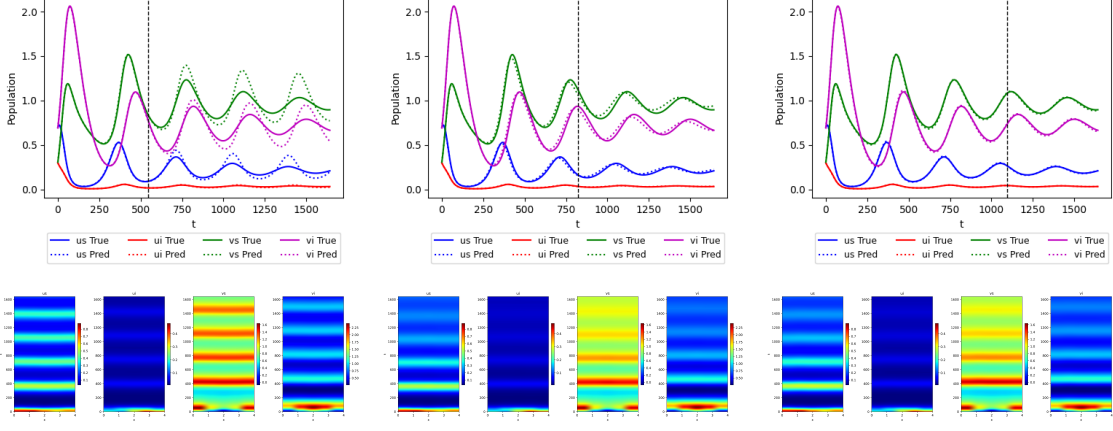


Figure 8: LVSIS: Comparison of prediction performance. Spatio-temporal model (1D)

Dynamics
Prediction

1/3

1/2

2/3

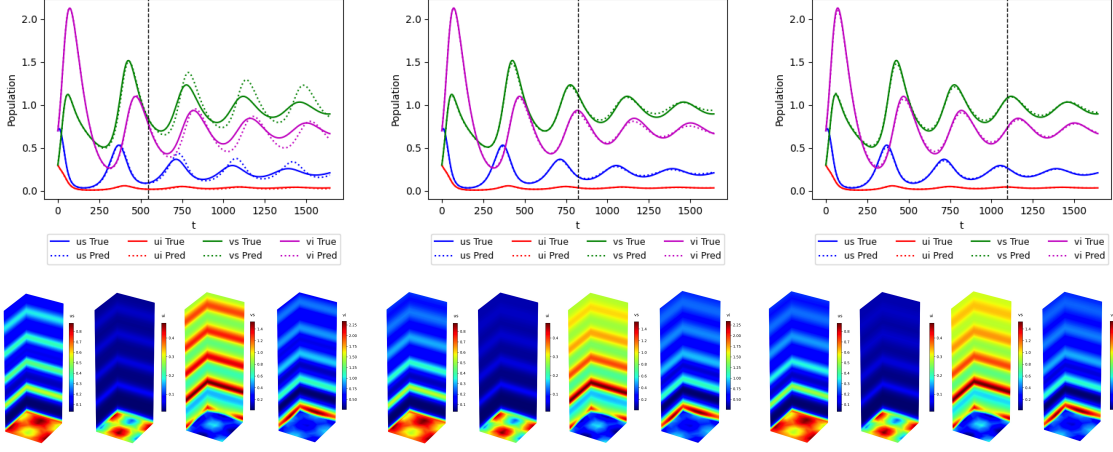


Figure 9: LVSIS: Comparison of prediction performance. Spatio-temporal model (2D)

window increases. The 2D model exhibits slightly higher errors than the 1D case, reflecting the increased complexity of learning spatial interactions in higher dimensions. The quantitative results in Table 5 are further illustrated in Figures 8 and 9, which compare the predicted dynamics with the reference solutions in 1D and 2D, respectively. In the 1D setting (Figure 8), the learned dynamics closely track the true solution even beyond the training window, while in the 2D case (Figure 9), minor discrepancies emerge during long-term extrapolation, particularly for shorter training horizons. Overall, the results demonstrate that we can effectively learn hidden local coupling mechanisms, with accuracy improving systematically as more temporal information is provided.

6 Conclusion

In this work, we explored data-driven approaches for learning eco-epidemiological dynamics from time-series data, focusing on three frameworks: Neural Ordinary Differential Equations (Neural ODEs),

Kolmogorov–Arnold Network ODEs (KANODEs), and the Sparse Identification of Nonlinear Dynamics (SINDy) method. Through numerical experiments on synthetic eco-epidemiological datasets, we demonstrated that all three approaches are capable of capturing the coupled nonlinear dynamics of the underlying systems. SINDy provides strong interpretability and physical insight by recovering sparse governing equations, closely aligning with traditional modeling paradigms. In contrast, Neural ODEs and KANODEs offer significantly greater adaptability, enabling them to accurately learn complex interactions that are difficult to encode explicitly and work with noisy data. Notably, KANODEs achieve comparable accuracy with substantially fewer trainable parameters, while deeper and wider Neural ODEs architectures consistently improve performance in more challenging settings, particularly for the LVSIS model. We further extended these methods to spatio-temporal systems and demonstrated that hidden local eco-epidemic coupling mechanisms can be successfully learned, while incorporating the diffusion operator as known physics. This hybrid formulation effectively combines data-driven learning with prior physical knowledge and enhances predictive capability in high-dimensional spatio-temporal problems.

Despite their strengths, the proposed approaches also exhibit several limitations. SINDy is highly sensitive to noise in the data and often requires careful preprocessing, such as smoothing or denoising, to produce stable and meaningful models. Neural ODEs and KANODEs, while more robust to noise, generally sacrifice interpretability and rely on computationally intensive training procedures. In particular, although KANODEs reduce the number of trainable parameters, their training cost can be significantly higher due to the complexity of the underlying architecture. Moreover, increasing model depth and width, while beneficial for accuracy, may lead to higher computational overhead. For spatio-temporal models, the assumption of known diffusion may not always be realistic, and extending the framework to simultaneously learn both reaction and transport operators remains an important open direction.

In future work, we plan to further advance the spatio-temporal direction by extending the proposed framework to more complex multiscale processes. In particular, we aim to leverage averaged (coarsened) algorithms combined with implicit–explicit (IMEX) coupling to enhance numerical stability and broaden the applicability of the proposed techniques to wider classes of problems [34, 35]. Accurate upscaling strategies will enable inexpensive yet reliable training on coarse representations, while preserving the ability to recover fully space–time–resolved solutions when needed. This research direction will involve the development and analysis of implicit and IMEX-inspired neural architectures [36, 37, 38, 39].

References

- [1] John Prenter, Calum MacNeil, Jaimie TA Dick, and Alison M Dunn. Roles of parasites in animal invasions. *Trends in ecology & evolution*, 19(7):385–390, 2004.
- [2] Roy M Anderson. Populations and infectious diseases: ecology or epidemiology? *Journal of Animal Ecology*, 60(1):1–50, 1991.
- [3] Min Su. Modeling at the interface of ecology and epidemiology. *Computational Ecology and Software*, 5(4):367, 2015.
- [4] Robert Leo Smith, Robert Leo Smith, Graham C Hickman, and Susan M Hickman. Elements of ecology. 1998.
- [5] Hyangim Ji, Maria Vasilyeva, Nana Adjoah Mbroh, and Alexey Sadovski. Epidemic dynamics in the spatio-temporal predator-prey model. *Frontiers in Applied Mathematics and Statistics*, 11:1642676, 2025.
- [6] A proposal on machine learning via dynamical systems. *Communications in Mathematics and Statistics*, 5(1):1–11, 2017.
- [7] Yonggi Park, Kelum Gajamannage, Dilhani I Jayathilake, and Erik M Boltt. Recurrent neural networks for dynamical systems: Applications to ordinary differential equations, collective motion, and hydrological modeling. *arXiv preprint arXiv:2202.07022*, 2022.

[8] Philemon Manliura Datilo, Zuhaimy Ismail, and Jayeola Dare. A review of epidemic forecasting using artificial neural networks. *Epidemiology and Health System Journal*, 6(3):132–143, 2019.

[9] Chrysoula Kosma, Giannis Nikolentzos, George Panagopoulos, Jean-Marc Steyaert, and Michalis Vazirgiannis. Neural ordinary differential equations for modeling epidemic spreading. *Transactions on Machine Learning Research*, 2023.

[10] Yuxi Huang, Huandong Wang, Guanghua Liu, Yong Li, and Tao Jiang. Neuralcode: Neural compartmental ordinary differential equations model with automl for interpretable epidemic forecasting. *ACM Transactions on Knowledge Discovery from Data*, 19(2):1–18, 2025.

[11] Xiao Ning, Linlin Jia, Yongyue Wei, Xi-An Li, and Feng Chen. Epi-dnns: Epidemiological priors informed deep neural networks for modeling covid-19 dynamics. *Computers in biology and medicine*, 158:106693, 2023.

[12] Xianglei Zhu, Bofeng Fu, Yaodong Yang, Yu Ma, Jianye Hao, Siqi Chen, Shuang Liu, Tiegang Li, Sen Liu, Weiming Guo, et al. Attention-based recurrent neural network for influenza epidemic prediction. *BMC bioinformatics*, 20(Suppl 18):575, 2019.

[13] Sangwon Chae, Sungjun Kwon, and Donghyun Lee. Predicting infectious disease using deep learning and big data. *International journal of environmental research and public health*, 15(8):1596, 2018.

[14] Benjamin Deneu, Maximilien Servajean, Pierre Bonnet, Christophe Botella, François Munoz, and Alexis Joly. Convolutional neural networks improve species distribution modelling by capturing the spatial structure of the environment. *PLoS computational biology*, 17(4):e1008856, 2021.

[15] Sovan Lek and Jean-François Guégan. Artificial neural networks as a tool in ecological modelling, an introduction. *Ecological modelling*, 120(2-3):65–73, 1999.

[16] Yves Moreau, Stéphane Louiès, Joos Vandewalle, and Léon Brenig. Embedding recurrent neural networks into predator–prey models. *Neural Networks*, 12(2):237–245, 1999.

[17] NDSL Tilahun, Saratha Sathasivam, and Ong Hong Choon. Prey-predator algorithm as a new optimization technique using in radial basis function neural networks. *Res J Appl Sci*, 8(7):383–387, 2013.

[18] Steven L Brunton, Joshua L Proctor, and J Nathan Kutz. Discovering governing equations from data by sparse identification of nonlinear dynamical systems. *Proceedings of the national academy of sciences*, 113(15):3932–3937, 2016.

[19] Ricky TQ Chen, Yulia Rubanova, Jesse Bettencourt, and David K Duvenaud. *Advances in neural information processing systems*, 31, 2018.

[20] Ziming Liu, Yixuan Wang, Sachin Vaidya, Fabian Ruehle, James Halverson, Marin Soljačić, Thomas Y Hou, and Max Tegmark. Kan: Kolmogorov-arnold networks. *arXiv preprint arXiv:2404.19756*, 2024.

[21] Benjamin C Koenig, Suyong Kim, and Sili Deng. Kan-odes: Kolmogorov–arnold network ordinary differential equations for learning dynamical systems and hidden physics. *Computer Methods in Applied Mechanics and Engineering*, 432:117397, 2024.

[22] Vladimir Igorevich Arnol'd. On functions of three variables. 114(4):679–681, 1957.

[23] Andrei Nikolaevich Kolmogorov. On the representation of continuous functions of several variables as superpositions of continuous functions of one variable and addition. 114(5):953–956, 1957.

[24] Ziyao Li. Kolmogorov-arnold networks are radial basis function networks. *arXiv preprint arXiv:2405.06721*, 2024.

[25] Liangwei Nathan Zheng, Wei Emma Zhang, Lin Yue, Miao Xu, Olaf Maennel, and Weitong Chen. Free-knots kolmogorov-arnold network: On the analysis of spline knots and advancing stability. *arXiv preprint arXiv:2501.09283*, 2025.

[26] Shao-Ting Chiu, Siu Wun Cheung, Ulisses Braga-Neto, Chak Shing Lee, and Rui Peng Li. Free-rbf-kan: Kolmogorov-arnold networks with adaptive radial basis functions for efficient function learning. 2026.

[27] Jonas A Actor, Graham Harper, Ben Southworth, and Eric C Cyr. Leveraging kanc for expedient training of multichannel mlps via preconditioning and geometric refinement. *arXiv preprint arXiv:2505.18131*, 2025.

[28] Brian M de Silva, Kathleen Champion, Markus Quade, Jean-Christophe Loiseau, J Nathan Kutz, and Steven L Brunton. Pysindy: a python package for the sparse identification of nonlinear dynamics from data. *arXiv preprint arXiv:2004.08424*, 2020.

[29] Maria Vasilyeva, Aleksei Krasnikov, Kelum Gajamannage, and Mehrube Mehrubeoglu. Multiscale method for image denoising using nonlinear diffusion process: local denoising and spectral multiscale basis functions. *Journal of Computational and Applied Mathematics*, page 116733, 2025.

[30] Leonid I Rudin, Stanley Osher, and Emad Fatemi. Nonlinear total variation based noise removal algorithms. *Physica D: nonlinear phenomena*, 60(1-4):259–268, 1992.

[31] Adam Paszke, Sam Gross, Francisco Massa, Adam Lerer, James Bradbury, Gregory Chanan, Trevor Killeen, Zeming Lin, Natalia Gimelshein, Luca Antiga, et al. Pytorch: An imperative style, high-performance deep learning library. *Advances in neural information processing systems*, 32, 2019.

[32] Pauli Virtanen, Ralf Gommers, Travis E Oliphant, Matt Haberland, Tyler Reddy, David Cournapeau, Evgeni Burovski, Pearu Peterson, Warren Weckesser, Jonathan Bright, et al. Scipy 1.0: fundamental algorithms for scientific computing in python. *Nature methods*, 17(3):261–272, 2020.

[33] Harkaran Singh and Joydip Dhar. *Mathematical population dynamics and epidemiology in temporal and spatio-temporal domains*. CRC Press, 2018.

[34] Maria Vasilyeva. Generalized multiscale finite element method for discrete network (graph) models. *Journal of Computational and Applied Mathematics*, 457:116275, 2025.

[35] Maria Vasilyeva, Ben S Southworth, Yunhui He, and Min Wang. Implicit-explicit scheme with multiscale vanka two-grid solver for heterogeneous unsaturated poroelasticity. *arXiv preprint arXiv:2508.12197*, 2025.

[36] Eldad Haber, Keegan Lensink, Eran Treister, and Lars Ruthotto. Imexnet a forward stable deep neural network. In *International Conference on Machine Learning*, pages 2525–2534. PMLR, 2019.

[37] Eldad Haber and Lars Ruthotto. Stable architectures for deep neural networks. *Inverse problems*, 34(1):014004, 2017.

[38] Lars Ruthotto and Eldad Haber. Deep neural networks motivated by partial differential equations. *Journal of Mathematical Imaging and Vision*, 62(3):352–364, 2020.

[39] Shaojie Bai, J Zico Kolter, and Vladlen Koltun. Deep equilibrium models. *Advances in neural information processing systems*, 32, 2019.